# Magnetism engineering in antiferromagnetic β-FeOOH nanostructures via chemically-induced lattice defects

*Martín Testa-Anta[1*], Ecem Tiryaki[2], Laura Bocher[3], Verónica Salgueiriño[2,4]*

[1]Institut de Ciència de Materials de Barcelona (ICMAB-CSIC), Campus de la UAB, 08193 Bellaterra, Spain

[2]CINBIO, Universidade de Vigo, 36310 Vigo, Spain

[3]Université Paris-Saclay. CNRS, Laboratoire de Physique des Solides, 91405 Orsay, France

[4]Departamento de Física Aplicada, Universidade de Vigo, 36310 Vigo, Spain

ABSTRACT. Elongated akaganéite (β-FeOOH) nanostructures were synthesized through a simple hydrothermal route, in which a careful selection of the experimental conditions allows for a tunable length and aspect ratio and concomitantly predetermines the magnetic response. An in-depth structural characterization using transmission electron microscopy (TEM), X-ray diffraction (XRD) and Raman spectroscopy, jointly with DC magnetic measurements, reveals a complex scenario where the interstitial $Cl^-$ content dictates the β-FeOOH thermal stability and leads to the formation of bulk uncompensated spins along the inner channels. The coexistence of different magnetic contributions is observed to result in a non-monotonic dependence of the coercivity and exchange bias field on both temperature and size, posing major limitations to the archetypical magnetic core-shell model generally assumed for nanostructured antiferromagnets. As a proof-of-concept, we further show how the β-FeOOH internal microstructure can be chemically manipulated through Cl$^-$ anion exchange, giving rise to a superparamagnetic (SPM) component that comes along with an almost 20-fold increase in the coercivity at low temperature. The evaluation of these results reveals the potential of controlling the interplay between crystal and magnetic structure via intercalation chemistry in antiferromagnets, expanding fundamental science knowledge and supporting practical applications, given their huge role in the technological fields of spintronics and magnonics.

## 1. INTRODUCTION

The recent progress on the electrical switching and ultra-fast dynamics of antiferromagnetic (AFM) systems has prompted the development of a new generation of spintronic-based devices,[1–6] spurring a profound interest in the fundamentals of antiferromagnetism. In fact, albeit the properties of many antiferromagnets are well-stablished in bulk form, there exists less consensus on the properties of the same materials at the nanoscale, where surface and finite-size effects, jointly with related phenomena such as spin canting, spin frustration and glassy magnetism, play a crucial role. One example is akaganéite (β-FeOOH), whose unique crystalline structure endorses this material with interesting magnetic, catalytic, electrochemical and adsorption properties.[7–10] From a magnetic standpoint, bulk β-FeOOH exhibits an AFM behavior but, in the case of the nano-sized material, the appearance of hysteretic behavior, superparamagnetism, an intrinsic exchange bias field or the so-called ‘thermo-induced magnetic moment’ points to a more complex scenario with the occurrence of several magnetic contributions.[11]

Most studies up to date have proposed an AFM-FM(ferromagnetic) core-shell model, where geometric frustration at the surface provides a correlated source of uncompensated spins. The subsequent small net magnetic moment can accordingly account for the previous observations in the case of ultrafine and high-aspect ratio nanocrystals, where surface effects become predominant.[12,13] An enhancement of these surface effects has been reported in silica-coated α-FeOOH[14] and β-FeOOH[15] nanorods, in the latter case reflected by the increase in coercivity and exchange bias field in comparison with the bare nanorods. However, despite the suitability of the model for these particular systems, the non-scalability of the different magnetic parameters with particle size, its strong dependence on the synthetic methodology and the concomitant lack of an in-depth structural characterization leave many open questions.

Aside from the size, shape and surface anisotropy, the presence of strain and crystallographic defects such as ionic vacancies, dislocations, twin or antiphase boundaries were also proved to serve and additional source of magnetic ordering.[16–21] A proper understanding of the spin order at these spatial regions is hence of major importance for materials science-based technologies, since the appropriate design of lattice defects can offer promising functionalities such as the pinning of domain walls and the induction of larger critical fields for magnetic saturation.[22–24] These phenomena have been primarily investigated in thin films, rendering the number of studies conducted on nanoparticles very scarce, in spite of being naturally characterized by the presence of structural defects. This owes to the inherent difficulties at their rational engineering and the fact that they typically become overshadowed by the shape and topological nature of the nanocrystal itself. In this context, tuning the chemistry of materials via ion exchange constitutes an effective strategy to induce structural modifications and defects formation under controlled conditions.[25] Such soft chemistry approach has been widely used in semiconductor nanocrystals by means of both cation and anion exchange processes.[26–28] In the case of magnetic oxides, a partial tuning of the atomic structure through cation exchange was recently reported in the surface of magnetite ($Fe_3O_4$) and wüstite ($Fe_xO$) nanocrystals,[29] but the compositional modifications unavoidably led to a core-shell structure with a detrimental effect on the magnetic properties registered. Another challenge involved in the post-synthetic substitution of magnetic cations relates to the Kirkendall effect, which often leads to hollow structures and prevents maintaining the parent morphology.[30] Most of these issues can be circumvented in akaganéite, whose peculiar tunnel structure was reported to allow the accommodation of a plethora of anions within the channels parallel to the *b*-direction, such as $Br^-$, $F^-$ or $OH^-$.[31] This provides a steady platform for anion exchange, in which a defective or distinctive anion occupation can generate inner (bulk) uncompensated spins that may govern the eventual magnetic response in nanoscaled antiferromagnets. These possibilities of tunable magnetism have been hypothesized in previous studies, yet no direct evidences have been provided, except for the work of Chambaere and De Grave.[32] In that work, the Néel temperature was found to decrease linearly with the interstitial water content, though no other magnetic parameters nor further structural considerations were investigated.

All things considered, and despite the efforts to disentangle the origin of frustrated antiferromagnetism, very few reports attempt to establish a correlation between magnetism and crystal structure in akaganéite nanocrystals. In this work, we take a first step to answer the fundamental question about the role of the interstitial $Cl^-$ anions on the lattice stability and its implications on the magnetic properties. To this end, we firstly show how the interplay between the different synthetic parameters predetermines not only the morphology, but also the interstitial

$Cl^-$ content. This content is analyzed from a Raman perspective and linked to the appearance of non-correlated spin disorder, leading to a FM-like component whose strength depends on its coupling to the AFM core. Finally, as a proof-of-concept, these ions were exchanged with hydroxide anions via a chemical wet method. The as-obtained results evidence unprecedented changes in the magnetic response without inducing a phase transformation during the $Cl^-/OH^-$ exchange. Overall, these results prove that the archetypical magnetic core-shell model does not satisfactorily reproduce the akaganéite AFM behavior, and disclose the huge potential of crystallographic defects at magnetism engineering in nanoscaled antiferromagnets.

## 2. EXPERIMENTAL SECTION

**2.1. Materials.** Iron(III) chloride hexahydrate ($FeCl_3.6H_2O$, ≥99%), sodium hydroxide (NaOH, ≥98%), hydrochloric acid (HCl, 37%) and absolute ethanol (EtOH, ≥99.9%) were purchased from Sigma-Aldrich. All chemicals were used as received without further purification. Distilled water was used in all aqueous preparations.

**2.2. Synthesis of β-FeOOH nanocrystals.** Elongated β-FeOOH nanostructures were synthesized through the forced hydrolysis of an $FeCl_3$ aqueous solution at elevated temperature. In a typical synthesis, a given amount of iron precursor ($FeCl_3.6H_2O$) was dissolved in distilled water and transferred to a tightly sealed autoclavable bottle. The recipient was then placed in a preheated electric oven and kept at a fixed temperature (60 or 100 °C) for 6 hours (refer to Table 1 for detailed experimental conditions). Upon cooling to room temperature, the nanoparticles were collected by centrifugation (3420 g, 20 min.) and washed through several redispersion-centrifugation cycles (three times with water followed by one additional washing step with ethanol). The resultant yellow-brown powder was dried for 48 hours at room temperature for further characterization. For the synthesis of high-aspect ratio β-FeOOH needles, an appropriate amount of HCl was added to the reaction mixture and the hydrolysis was allowed to continue over 18 hours, as reported in a previous work.[7]

**2.3. $Cl^-$ anion exchange.** A partial removal of chloride anions from the akaganéite tunnel structure was accomplished via $Cl^-/OH^-$ anion exchange, according to a slightly modified protocol described elsewhere.[31] Namely, 20 mg of β-FeOOH powder were dispersed in 100 mL of 0.5 M NaOH solution, and subsequently heated to 55 °C under magnetic stirring. After 3 hours, the anion-exchanged β-FeOOH nanostructures were separated by centrifugation and washed following the workup procedure described before.

**2.4. Characterization.** Samples for transmission electron microscopy (TEM) were prepared by dropping a dilute dispersion of the nanoparticles onto a carbon-coated 400-mesh copper grid. TEM images were obtained with a JEOL JEM1010 microscope operating at an acceleration voltage of 100 kV. Size histograms were obtained by manual counting over 200 particles (considering both length and diameter). The corresponding size distributions were fitted to a log-normal function, expressing the final results in terms of the arithmetic mean and standard deviation as $x \pm 2\sigma$ (i.e. for a 95.5% interval of confidence). High-angle annular dark-field (HAADF) images were acquired with a C3/C5-corrected Nion UltraSTEM 200 operated at 100 kV with a 30 mrad convergence angle, and approximately 50 pA of probe current. X-ray diffraction (XRD) patterns were collected from powdered samples with a Panalytical X'Pert Pro diffractometer using Cu $K_\alpha$ radiation (Bragg-Brentano $\theta$-$2\theta$ geometry) in the $2\theta$ angular range of 10-80° and a continuous scan mode (step = 0.02°, 4 seconds/step). Raman spectra were collected with a Renishaw in Via Reflex confocal system. Experiments were conducted at room temperature using a 785 nm NIR diode laser. The laser beam was focused onto the sample with a 20x objective (N.A. 0.40), and the Raman spectra were registered in backscattering geometry using a high-resolution grating (1200 grooves $mm^{-1}$). The laser power was varied in the 0.27-29 mW range and the acquisition time was set to 120 seconds. Magnetic measurements were performed using the VSM option in a PPMS and MPMS-3 system from Quantum Design. The temperature-dependent magnetization in zero-field-cooling (ZFC) and field-cooling (FC) conditions was recorded applying either a 10 or 500 mT magnetic field in a temperature range between 10-350 K. Hysteresis loops were registered at different temperatures (in the 10-300 K range) applying an external magnetic field up to 5 T. FC hysteresis loops were measured after cooling the sample from 340 K in a 5 T magnetic field. Owing to the low coercivity of the samples herein described, the field-dependent magnetization was corrected with the true field calculated from a Pd standard data at 298 K. All magnetic measurements were performed on dried samples using conventional VSM powder and brass half-tube sample holders.

## 3. RESULTS AND DISCUSSION

**3.1. Synthesis of β-FeOOH nanocrystals and growth mechanism.** A series of akaganéite (β-FeOOH) nanocrystals were synthesized via thermal hydrolysis of an adequate iron precursor ($FeCl_3.6H_2O$) following the experimental conditions detailed in Table 1. A transmission electron microscopy (TEM) analysis of these samples (included in Figure 1a-f) revealed the presence of elongated nanostructures, with average length 330 ± 30 nm (Ak-60), 638 ± 92 nm (Ak-100) and 3.06 ± 2.87 μm (Ak-needle), and aspect ratios of 4.1, 5.5 and 31.2, respectively (see corresponding distribution profiles in Figure 1g-i). In contrast to other methods reported in the literature, the absence of shape-control and capping agents (such as dopamine[15], polyethyleneimine[33] or glucose[34]), a polymer-based matrix[35] or ultrasonic-irradiated synthesis[9] results in nanostructures with lengths of several hundreds of nanometers. In order to account for the different size and morphology, various parameters such as the concentration of iron precursor and chloride ions, pH, aging time and temperature are expected to play a crucial role.

The formation of akaganéite is preceded by the hydration of $Fe^{3+}$ cations to form the hexa-aqueous iron(III) complex $[Fe(H_2O)_6]^{3+}$, which undergoes subsequent hydrolysis reactions depending on the pH of the medium:

$$[Fe(H_2O)_6]^{3+} + nH_2O \rightleftharpoons [Fe(OH)_n(H_2O)_{6-n}]^{3-n} + nH_3O^+ \quad (1)$$

The condensation of these complexes will boost the formation of β-FeOOH nuclei through successive oxolation and/or olation reactions, where both kinetic and thermodynamic considerations dictate the final morphology. As reported in previous studies, the solubility or saturation concentration of $Fe^{3+}$ species significantly increases at low pH.[36] This will reduce the volume Gibbs free energy stabilization and impose a higher energy barrier for the nucleation process, requiring a higher supersaturation before the nucleation takes place. As a consequence, the monomer concentration will drop rather quickly below the nucleation level and prompt the particle growth until it further decreases below the saturation threshold.[7,13] Contrary to the classical LaMer picture, where a quick outburst of nucleation is pursued, the primary effect of this constrained nucleation will be the presence of fewer and larger nanoparticles. This fact can be corroborated when comparing the sample synthesized in the presence of 0.07 M HCl (Ak-needle) with those synthesized in the absence of HCl (Ak-60 and Ak-100). The pH is found to be concomitantly bound to the concentration of $FeCl_3$, given that the iron(III) complexes indicated in eq. 1 are inherently acidic. Hence, the quantitatively higher amount of iron precursor utilized during the synthesis of the Ak-needle sample will also contribute to halt the nucleation and boost diffusional growth in light of the excess of iron species existing in solution.

The morphological dissimilarities between the Ak-60 and Ak-100 samples must originate from the reaction temperature instead. Elevated temperatures are known to accelerate the hydrolysis rate of the iron complexes in eq. 1[37] and lower the energy barrier for nucleation. This will lead to a faster nucleation rate, such that a large number of small nuclei, and eventually small particles, should be anticipated. The fact that the particles synthesized at 100 °C (Ak-100) display a much larger size than those synthesized at 60 °C (Ak-60) points therefore to different growth mechanisms, as depicted in Figure 1j. Bearing in mind the lower reaction temperature in the Ak-60 case, its growth is seemingly governed by a diffusion-controlled mechanism, in accordance with LaMer model and the higher monodispersity obtained for this sample (refer to Table 1 for standard deviation values). On the contrary, the diffusion coefficient of the iron species will drastically increase at 100 °C, such that particle growth will essentially proceed through a surface-controlled mechanism. Accordingly, the diffusion enhancement in the Ak-100 sample accounts for their larger size (almost twice in length in comparison to Ak-60) and the concomitant increase in size dispersion registered, as this mechanism always leads to particle size broadening.

Equally important is the role of the aging time. A priori longer nanoparticles will be obtained with longer reaction times, since more diffusion and monomer attachment will be allowed to occur. If considering a surface-controlled growth, prolonged hydrolysis times will be accompanied by a broader size distribution. These two facts are realised in the Ak-needle sample. Conversely, the slower growth dynamics for a diffusion-controlled mechanism (like in the Ak-60 sample) seem to reach a maximum length of ~700 nm for sufficiently long aging times (6 days) without compromising the particle size distribution. Long reaction times at 100 °C were seen to favor the formation of hematite via a dissolution-reprecipitation process.[36] In fact, under the same synthetic conditions of the Ak-needle sample, hematite traces could be already detected upon 24 hours.

Remarkably, in the Ak-100 sample a large proportion of akaganéite nanoparticles is observed to assemble into rafts, with their long axes parallel to each other (see Figure S1 in the Supporting Information, SI). The parallel aggregation likely stems from the strong van der Waals interactions established between the nanostructures because of their high Hamaker constant in water, as reported for other iron oxides and oxyhydroxides.[7] Additionally, the formation of stacks can be promoted by the presence of weak magnetic moments within the nanoparticles originating from a frustration of the antiferromagnetic ordering. This frustration has been reported to provide directionality in silica-coated akaganéite needles, by aligning their short axes parallel to an external magnetic field.[7] On that basis, the stronger interactions in Ak-100 hint a larger net magnetic moment per particle in this sample. The absence of orientational behavior in the Ak-needle sample can be related to the higher electrostatic repulsion resulting from the increased [$Cl^-$] concentration or to a degraded magnetic behavior.

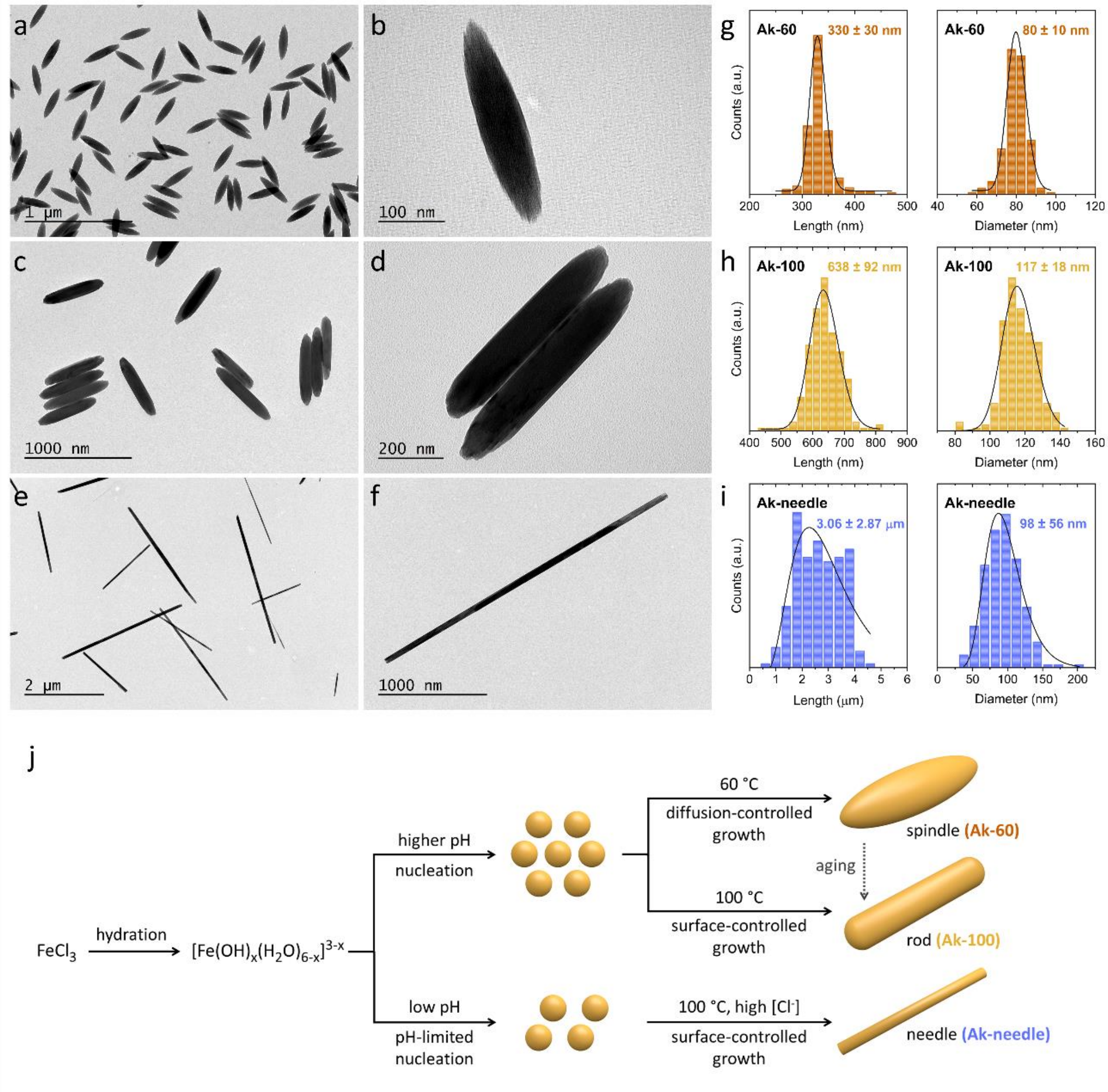

**Figure 1.** Representative TEM images obtained at low (a, d, g) and high (b, e, h) magnification, and particle size distribution (c, f, i) for the three akaganéite samples synthesized (Ak-60, Ak-100 and Ak-needle, respectively). (j) Scheme of the mechanism herein proposed for the growth of β-FeOOH nanostructures, showing the different synthetic pathways and resultant morphologies as a function of pH, temperature and aging time.

**Table 1.** Summary of the experimental conditions used during the hydrolysis of the $FeCl_3$ solutions, and resultant particle dimensions as determined by TEM analysis.[a]

| Sample | [$FeCl_3$] (M) | [HCl] (M) | Temp. (°C) | Time (h) | Length, L | Diameter, D | L/D |
|---|---|---|---|---|---|---|---|
| Ak-60 | 0.10 | 0 | 60 | 6 | 330 ± 30 nm | 80 ± 10 nm | 4.1 |
| Ak-100 | 0.10 | 0 | 100 | 6 | 638 ± 92 nm | 117 ± 18 nm | 5.5 |
| Ak-needle | 0.60 | 0.07 | 100 | 18 | 3.06 ± 2.87 μm | 98 ± 56 nm | 31.2 |

[a] The mean particle length (L) and diameter (D) were determined by fitting the corresponding size distributions to a log-normal function, and appear expressed in terms of the arithmetic mean and standard deviation as $x \pm 2\sigma$ (for an interval of confidence of 95.5%).

**3.2. Structural Characterization.** The crystal structure of the akaganéite phase has been a matter of extensive debate in the literature. Early studies described the β-FeOOH crystallographic properties in terms of a tetragonal system with I4/m symmetry,[38,39] whereas more recent and precise Rietveld refinements based on synchrotron X-ray and neutron diffraction data corroborated a monoclinic unit cell with space group I2/m.[40] The crystal lattice can be described as a hollandite-like structure consisting of double chains of two distinct edge-sharing $Fe(O,OH)_6$ octahedra, which results in two non-equivalent Fe and four non-equivalent O sites (4i Wyckoff position).[40,41] These double chains are found to be interconnected through corner-sharing with adjacent chains, rendering a tunnel-like structure with channels lying parallel to the *b*-direction (as shown in Figure 2a, left scheme). Each of these channels possesses a square cross section measuring two octahedral units in length (~0.4 nm),[42] and displays a partial occupation of $Cl^-$ anions (~2/3 of the tunnel sites) stabilized by hydrogen bonds.[43] The $Cl^-$ anions reside near the center of the prism defined by the eight H atoms belonging to the hydroxyl groups (4g Wyckoff position; depicted in Figure 2a, right scheme). On the other hand, three different H sites can be identified: two of them stemming from two non-equivalent hydroxyl groups (8j Wyckoff position) and a third one ascribable to an additional H atom within the tunnels (4i Wyckoff position).[40] Considering the previous crystallographic arrangement, Post et al. calculated the lattice parameters to be $a$= 10.588 Å, $b$= 3.034 Å, $c$= 10.528 Å and β= 90.14°,[40] though some discrepancies can be found in the case of fine β-FeOOH particles as a result of different Cl occupancies (see for instance ref. [41]).

The XRD patterns from the as-prepared samples (included in Figure 2b) reveal the presence of the pure akaganéite phase (JCPDS cards no. 34-1266 and 42-1315 for I4/m and I2/m symmetries, respectively). Interestingly, despite displaying a much larger size, the diffraction peaks from the Ak-needle sample are observed to broaden, hinting smaller crystalline domains due to Scherrer broadening and/or a reduced crystallinity. A high-resolution TEM characterization from the Ak-60 sample further discloses the inherent polycrystallinity of the akaganéite nanostructures, as reflected by the diffraction rings in the corresponding FFT pattern (see Figure S2). The diffuse diffraction spots perpendicular to the elongation direction indicate the presence of nanocrystallites with slightly different $a/c$ lattice parameter ratio which are oriented along the $b$-axis (for I2/m symmetry). Significant variations can be also noted in the ratio of the $(10\bar{1})$ and $(30\bar{1})$ reflections. This ratio is calculated to be 0.68, 0.76 and 1.03 for the Ak-60, Ak-100 and Ak-needle samples, respectively. This trend can be understood in terms of a preferred orientation, since the $(10\bar{1})$ relative intensity increases along with the aspect ratio of the nanostructures. Note that the $[10\bar{1}]$ direction is perpendicular to the elongation direction in the monoclinic I2/m space group ($b$-axis).

In contrast to other iron oxide and oxyhydroxide phases, very few studies elaborate on the Raman characterization of akaganéite. This possibly stems from the inherent difficulties in the preparation of the single crystalline material[12] as well as from the large number of Raman active modes for this monoclinic crystal lattice $(21\mathrm{A_g} + 15\mathrm{B_g})$ and their proximity in frequency, which prevents us from carrying out an accurate assignment of each phonon symmetry. The most complete spectra in the literature generally identify ten band positions for akaganéite in the 100-900 $cm^{-1}$ region,[42] being the most intense those located at approximately 310 and 385 $cm^{-1}$. These spectral features in the low-wavenumber region are related to Fe-O stretching and Fe-OH bending vibrations at the $Fe(O,OH)_6$ octahedral sites.[44] The presence of two Fe and four O non-equivalent sites accounts for the wide range of Fe-O bond distances and, consequently, of Fe-O vibrations, which presumably merge into broad and asymmetric bands due to their similar energy. These spectral fingerprints and their relative intensity allow however to easily discriminate between akaganéite and other oxyhydroxide polymorphs, such as lepidocrocite (γ-FeOOH) or goethite (α-FeOOH), which are typical products resulting from the hydrolysis of iron salts. Figure 2c includes the Raman spectra of the three akaganéite samples synthesized (Ak-60, Ak-100 and Ak-needle), registered with a 785 nm excitation wavelength and a laser power of 0.51 mW. Taking the Ak-60 sample as reference, nine main features can be appreciated at $\sim$115, 140, 310, 386, 414, 490, 536, 608 and 723 $cm^{-1}$, which are in agreement with the values reported in the literature for the same material.[42,44] In addition to the aforementioned features in the 100-900 $cm^{-1}$ region, a subtle asymmetry is present at $\sim$250 $cm^{-1}$. This feature was systematically observed in the three samples herein considered and can be appreciated in most of the Raman spectra in the literature.[42,45,46] Albeit it may be indicative of lepidocrocite (γ-FeOOH), whose Raman fingerprint includes a sharp and intense peak at 250 $cm^{-1}$,[45,47,48] its low intensity and the large overlapping degree between the numerous akaganéite vibrational modes suggest that this feature must be inherent to the akaganéite phase.

Table 2 summarizes the Raman band positions of the different akaganéite samples and the relative intensity ratios of the bands at 310, 386 and 414 cm$^{-1}$ (see Figure S4 for spectra deconvolution). A comparative analysis of the three samples reveals no significant changes in the position of the bands, but it does unveil some differences in their relative intensity, particularly noticeable for the bands at 386 and 414 cm$^{-1}$. Indeed, whereas the intensity ratio of the bands at 310 and 386 cm$^{-1}$ is found to be very similar in the three cases (ca. 0.90), the ratio of the 386 and 414 cm$^{-1}$ contributions is calculated to be 1.16, 1.33 and 2.95 for the Ak-60, Ak-100 and Ak-needle samples, respectively. These variations can be explained by different Cl$^-$ contents in the three akaganéite samples, as previously reported by Réguer and co-workers.[44] Based on that work, the trend observed points to a higher chloride content in the Ak-needle sample and lower in the Ak-60 sample. According to previous studies in the literature, the insertion of Cl$^-$ anions within the β-FeOOH framework is charge-balanced by the addition of H cations,[40,49] resulting in a FeO$_{0.833}$(OH)$_{1.167}$Cl$_{0.167}$ stoichiometry. This chemical composition entails a theoretical Cl$^-$ content of 6.2 wt. %, in agreement with typical values reported in the literature for synthetic akaganéite (4.5-12.0 wt. %).[50] The presence of Cl$^-$ anions adsorbed at the surface of the β-FeOOH particles is not expected to modify their (bulk) vibrational structure. Hence, the changes in the I$_{386}$/I$_{414}$ ratio necessarily imply different interstitial Cl$^-$ contents.

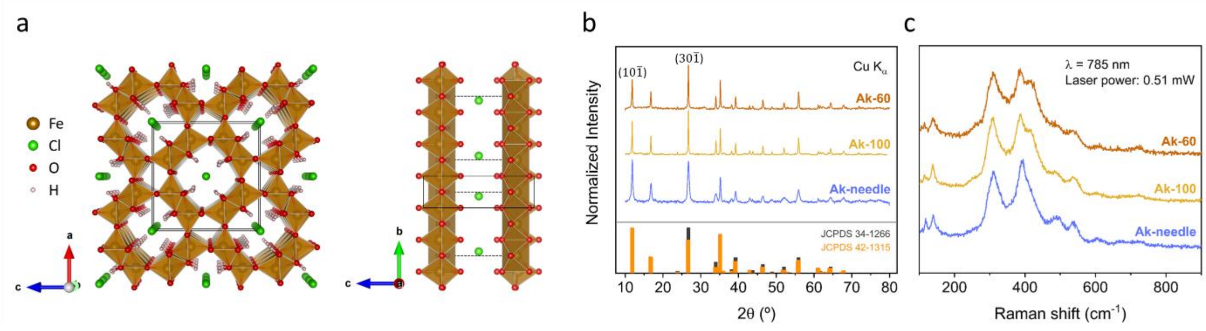

**Figure 2.** (a) Polyhedral representation of the akaganéite crystal structure viewed down the *b*-axis (left scheme), or perpendicular to the *b*-direction showing the $Cl^-$ anion ordering scheme within the inner channels (right scheme). The black dotted lines reflect the displacement of the $Cl^-$ anions with respect to the (0,0,0) position. Room-temperature powder XRD patterns (b) and Stokes-shifted Raman spectra (c) of the akaganéite samples synthesized. Note that the $(10\bar{1})$ and $(30\bar{1})$ reflections have been indexed according to the monoclinic I2/m space group (which is equivalent to (110) and (310) in the tetragonal I4/m space group).

**Table 2.** Comparison of the Raman shift and relative intensity of the main bands observed in the akaganéite samples Raman spectrum.[a]

| Sample | Raman shift ($cm^{-1}$) | $I_{310}/I_{386}$ | $I_{386}/I_{414}$[b] |
|---|---|---|---|
| Ak-60 | 115, 140, 310, 386, 414, 490, 536, 608, 723 | 0.91 | 1.16 |
| Ak-100 | 115, 139, 309, 387, 414, 487, 536, 604, 723 | 0.92 | 1.33 |
| Ak-needle | 118, 140, 310, 392, 424, 490, 536, 604, 723 | 0.83 | 2.95 |

[a] All spectra were registered using a 785 nm excitation wavelength and applying a laser power of 0.51 mW. [b] Values determined upon band deconvolution using Lorentzian functions (see Figure S4 in the SI for more details).

With the aim of shedding some light on the thermal stability of the akaganéite crystal structure, a series of laser power-dependent Raman spectra were registered from the three samples (see Figure 3b-d). As expected, at higher laser powers the broad and asymmetric Raman signatures from akaganéite evolve to sharper and more symmetric peaks. Taking the Ak-60 sample as reference, these peaks occur at 226, 245, 293, 299, 411, 498 and 612 $cm^{-1}$, in agreement with the values reported for the $A_{1g}(1)$, $E_g(1)$, $E_g(2)$, $E_g(3)$, $E_g(4)$, $A_{1g}(2)$ and $E_g(5)$ modes from hematite, respectively.[48] This transition to hematite is observed to happen at a laser power threshold that significantly varies depending on the sample considered. The samples synthesized in the absence of HCl (Ak-60 and Ak-100) are seen to retain the akaganéite crystal structure up to 1.8 mW, being the transition to hematite fully completed at 8.1 mW. This thermally-induced transformation is known to proceed through the release of water, according to the following reaction:

$$2\beta\text{-FeOOH} \rightarrow \alpha\text{-Fe}_2\text{O}_3 + \text{H}_2\text{O} \quad (2)$$

Although thermodynamic considerations anticipate the formation of hematite, the kinetics of the dehydration/dehydroxylation mechanism (depicted in Figure 3a) can favor the formation of intermediate or metastable phases. In this regard, the goethite polymorph is known to directly transform to hematite, whereas lepidocrocite evolves to maghemite.[51] The spectra included in Figure 3b-d indicate that in all cases the transformation from akaganéite to hematite does not seem to proceed through any intermediate phase. It is noteworthy to mention that this transition is not a simple topotactic transformation (unlike the goethite-hematite and lepidocrocite-maghemite transformations), since it involves diffusion and mass transport and unavoidably results in the presence of defects and polycrystalline hematite samples.[52] An ion chromatography analysis of the akaganéite samples after annealing in air also revealed an effective removal of the interstitial $Cl^-$ ions during their transformation to hematite, reportedly released in the form of HCl.[53]

Compared to Ak-60 and Ak-100, the Ak-needle sample is observed to display an increased thermal stability. Though the full transition to hematite takes place at 8.1 mW (like in the Ak-60 and Ak-100 cases), the Raman spectrum of this sample does not undergo appreciable changes even at laser powers as high as 4.4 mW. We believe that this particular behavior provides solid evidence of the different interstitial $Cl^-$ contents among the samples. The $Cl^-$ anions are known to stabilize the akaganéite crystal structure via hydrogen bonding within the channels, leading to two different

O-H···Cl bonding schemes: a weaker linear hydrogen bond, occurring when one of the adjacent Cl sites is vacant, and a stronger bifurcated hydrogen bond, present when the Cl sites at both sides of the H atom are occupied.[40] On the basis of this crystallographic arrangement, a deficient $Cl^-$ occupation will decrease the number of bifurcated hydrogen bonds and ultimately decrease the stability of the akaganéite structure, lowering its transition temperature to hematite. The enhanced thermal stability of the Ak-needle sample comes therefore in agreement with the higher intensity ratio between its 386 and 414 $cm^{-1}$ Raman components, previously ascribed to a higher chloride content in this sample.

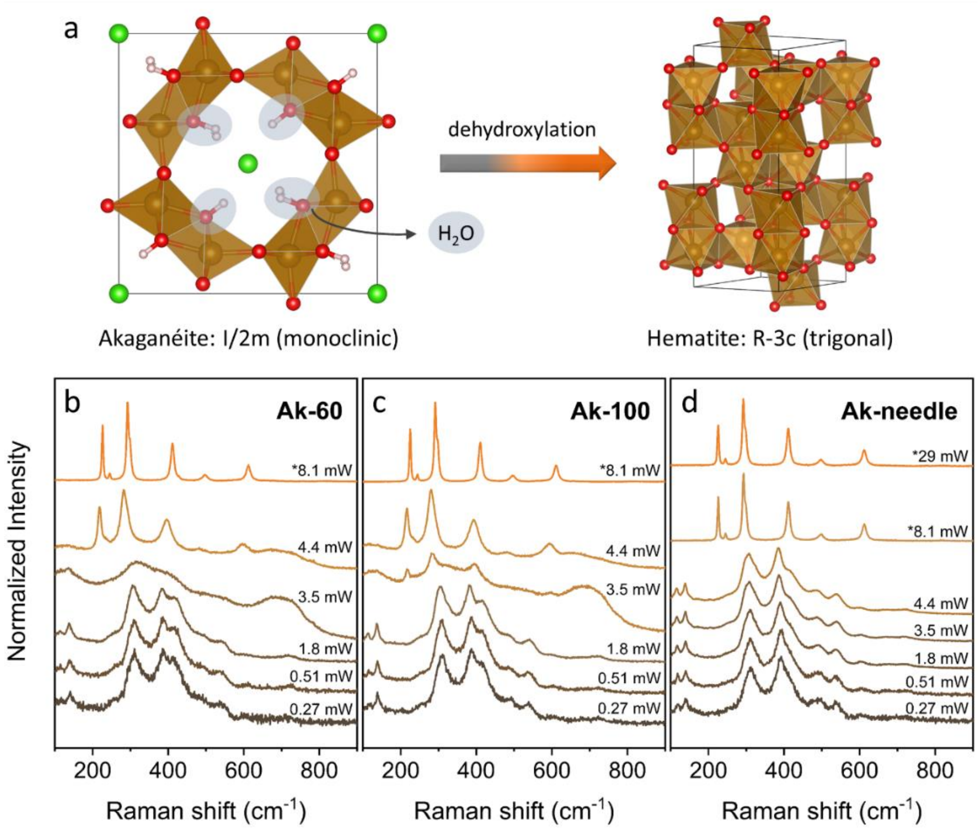

**Figure 3.** (a) Scheme of the thermal dehydroxylation and non-topotactic structural transformation from akaganéite (β-FeOOH) to hematite (α-$Fe_2O_3$). Laser power-dependent Raman

spectra of the Ak-60 (b), Ak-100 (c) and Ak-needle (d) samples. In all cases, the Raman spectra were registered from the same spot in the sample upon gradually increasing the laser power.

**3.3. Magnetic Properties.** The temperature-dependent magnetization, measured under ZFC and FC conditions (applying a constant 500 mT field), is included in Figure 4a-c. The as-registered curves reveal the presence of a maximum at 254 K for the Ak-60 and Ak-100 samples. Supported by the thermal dependence of the inverse susceptibility (see Figure 4d-f), this maximum is ascribed to the Néel transition temperature ($T_N$). The Curie-Weiss law predicts a linear behavior of the inverse susceptibility in the paramagnetic regime. Hence, the deviations from linearity observed at $T>T_N$ unveil the coexistence of several magnetic contributions. The Néel transition of the akaganéite phase has been reported to occur over a wide range of temperatures (typically between 240-299 K)[15] for differently synthesized β-FeOOH nanocrystals, and in some cases it cannot be directly resolved in the ZFC-FC curves. The fact that both the Ak-60 and Ak-100 samples display the very same $T_N$ points to bulk-like (i.e. size-independent) antiferromagnetic behavior. The presence of uncompensated spins (either at the surface and/or bulk material) in both samples can be inferred from the systematic increase in magnetization for $T<T_N$, causing the occurrence of a dip in the ZFC-FC curves. Note that the typical 3D-AFM thermal dependence would imply a continuous decrease of the magnetization below $T_N$ until reaching $\sim 2/3 M_{max}$ (when $T \rightarrow 0$ K).[54] Also, the irreversibility between the ZFC and FC curves at low temperatures indicates a ferromagnetic-like interaction involving these uncompensated spins, stronger in the Ak-100 than the Ak-60 sample. This is evidenced by the larger bifurcation between the two curves in the Ak-100 case, meaning that a larger magnetic field is required to align the uncompensated spins along the external field direction during the heating procedure.

An alternative behavior can be appreciated for the Ak-needle sample, which exhibits a Néel transition temperature of about 299 K. The broad maximum in the ZFC trace presumably stems from the broad size distribution of this sample compared to Ak-60 and Ak-100, whereas the pronounced dip in the 50-100 K range possibly correlates with the abrupt decrease in coercivity registered in this temperature range (see Figure S6c). Another plausible explanation relates to the occurrence of spin-glass behavior, favored by the reduced crystallinity of this sample and further suggested by the remarked ZFC-FC irreversibility (despite the negligible coercive field of this sample). Khalid et al. reported a similar value in high-aspect ratio β-FeOOH nanocrystals, where the $T_N$ of 2.2 μm-long nano-sticks could be ascertained at 285 K.[13] Taking into account that the Ak-60 and Ak-100 exhibit bulk-like AFM behavior[11] and the plethora of $T_N$ values reported in the literature for similarly sized materials, the increase in $T_N$ observed for the Ak-needle sample must be driven by a different mechanism. The pioneer work from Chambaere et al.[32] suggested a correlation between $T_N$ of the akaganéite phase and the interstitial water content. These authors claimed an increase in $T_N$ observed for decreasing amounts of crystal water until reaching a saturation $T_N$ of ~299 K in the limit of interstitial water-free nanocrystals. This water content was demonstrated to increase over prolonged hydrolysis times and high reaction temperatures. Therefore, notable differences are a priori expected between the $T_N$ from the Ak-60 and Ak-100 samples, which is not the case. An alternative explanation relates to the occurrence of hematite traces in the Ak-needle sample. The presence of this phase could be detected after a 24-hour hydrolysis time (see Figure S5 in the SI), but no signature of this oxide was observed at 18 hours neither by Raman spectroscopy nor XRD. If present, there must be in the form of very small crystalline domains, below the detection limit of both techniques. All the facts above point instead to the interstitial Cl$^-$ ions as the predominant underlying mechanism at dictating the magnetic properties.

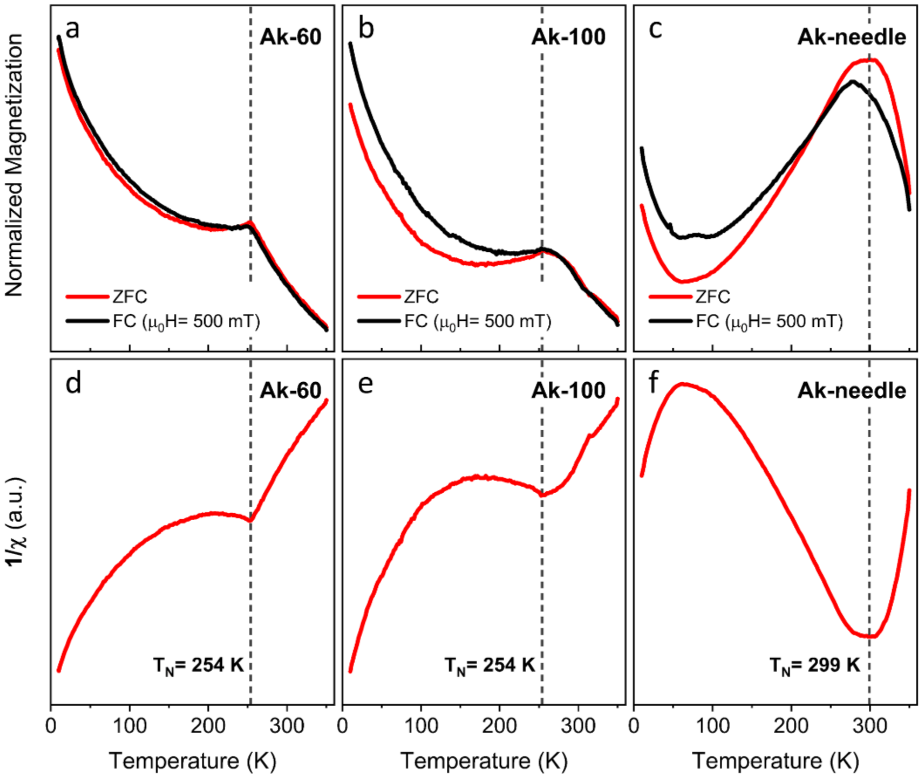

**Figure 4.** Temperature-dependent magnetization curves registered in zero-field cooling (ZFC) and field-cooling (FC, $\mu_0H$= 500 mT) conditions, and variation of the inverse ZFC magnetic susceptibility with temperature for the samples Ak-60 (a, d), Ak-100 (b, e) and Ak-needle (c, f), respectively.

The field-dependent magnetization curves of the three samples herein considered are included in Figure 5a-c, revealing in all cases the coexistence of two magnetic contributions: the main antiferro-/paramagnetic contribution (responsible for the linear dependence and non-saturation of the magnetization at the maximum applied field), jointly with a ferromagnetic-like response (see the zoom at around the low field region in Figure 5d-f for a better appreciation of the hysteretic behavior). Even though bulk akaganéite is agreed to exhibit an antiferromagnetic behavior, less consensus involves the origin of uncompensated spins in the nanosized material. The imbalance in the number of spins from the two magnetic sublattices due to symmetry disruption at the surface is typically evoked as the underlying source of uncompensated spins. On that basis, antiferromagnetic nanocrystals are often described in terms of a core-shell structure, consisting of a fully coherent and compensated AFM core and a ferro-/superparamagnetic (FM/SPM) surface. Nevertheless, despite the remarked shape anisotropy of the as-prepared samples, their surface-to-volume ratio (ca. 0.056, 0.037 and 0.041 for the Ak-60, Ak-100 and Ak-needle samples, respectively) is moderately low to assume a predominant surface contribution. This hypothesis is further supported by the following observations: i) the FM-like contribution does not correlate with the particle size nor the surface-to-volume ratio (see Table 3); ii) the strong synthetic dependence of the coercivity and interstitial $Cl^-$ content; and iii) the non-monotonic thermal variation of the coercive and exchange bias fields (refer to Figure S6), which hints a more complex scenario than the occurrence of two well-differentiated magnetic phases. Therefore, it becomes reasonable to assume that the uncompensated spins do not originate exclusively at the surface, but also at the core (bulk) of the nanocrystals. These inner magnetic defects may be induced by a distinctive chloride occupancy and the consequent crystallographic modifications in the akaganéite structure.

The coercive field ($\mu_0 H_C$) from the ZFC loops is measured to be 4.4, 19.9 and 2.5 mT at 10 K for the Ak-60, Ak-100 and Ak-needle samples. Despite the plethora of studies reporting on the preparation of β-FeOOH nanostructures, only a small number has directly assessed their hysteretic behavior. Typical coercive fields obtained for fine β-FeOOH particles are ∼45 mT (at 10 K, for spherical particles of 3.3 nm in diameter)[12] and 12.5 mT (at 50 K, for nanorods with a 80 nm length and 15 nm diameter),[15] whereas a coercivity of 22.5 mT (at 50 K) was reported for high aspect ratio nano-sticks (measuring 2.2 μm in length and 116 nm in diameter).[13] Most of the previous examples are characterized by large surface-to-volume ratios, where the predominant surface contribution is corroborated by the significantly larger magnetization observed at high fields[12] or the coercivity enhancement upon silica coating[15]. In our case, we have obtained coercive fields on the same order of magnitude (in particular for the Ak-100 sample), despite the much bigger dimensions of the nanostructures herein reported. The higher coercivity of the Ak-100 sample discloses a source of spin disorder in which the inner uncompensated spins are more strongly coupled to each other or to the bulk AFM component. Aiming to shed light on this contribution, the magnetization was plotted as a function of the variable $\mu_0 H/T$ for a fixed temperature (see Figure S7). It can be noted that the curves obtained at different temperatures do not superimpose, opposed to what would be expected for a (super-)paramagnetic behavior, governed by the Langevin equation. The absence of SPM behavior concurs with the non-observation of a clear blocking temperature in the ZFC-FC curves. Henceforth, our results allow to discard an effective exchange interaction between the inner uncompensated spins and unveil a non-correlated spin disorder scenario where these spins are more strongly (Ak-100) or weakly (Ak-60) coupled to the main AFM order. On the contrary, the nearly vanishing coercivity of the Ak-needle sample and the significant decrease in magnetization (~46% compared to Ak-60) at the maximum applied field (5 T) may be indicative of spin-glass behavior, probably boosted by the inherent structural disorder of this remarkedly polycrystalline sample.

The FC hysteresis loops were additionally measured after cooling the sample from 350 K in a 5 T magnetic field, as shown in Figure 5g-i. The corresponding values of exchange bias field ($\mu_0 H_E$) at 10 K are -21.9, -9.0 and -37.6 mT for the Ak-60, Ak-100 and Ak-needle samples, respectively.

These values are consistent with those reported in the literature for smaller nanostructures, generally in the 7-40 mT range.[12,13,15,55] In line with atomistic simulations performed on core-shell FiM(ferrimagnetic)-AFM nanoparticles,[56] a stronger(weaker) interfacial coupling is observed to produce an increase(decrease) in coercivity and a decrease(increase) in the exchange bias field. Note that the 'interfacial' term is herein employed from a magnetic perspective, highlighting the exchange interaction between two different magnetic components, and not from the occurrence of two structurally incoherent crystallographic phases. From the thermal evolution of the magnetic parameters (see Figure S6), the coercivity of the Ak-100 sample is seen to decrease as the temperature increases, following the typical ferromagnetic behavior. No important changes can be detected in this sample for the coercivity under ZFC and FC conditions. This clearly reinforces the absence of a significant proportion of pinned uncompensated spins (which do not rotate with the external field), presumably due to the presence of a lesser amount of structural defects. These pinned uncompensated moments were reported to influence the exchange bias in AFM materials,[57] and thus could also help explain the lower $\mu_0 H_E$ obtained in Ak-100. For the Ak-needle sample, on the other hand, the systematic increase in coercivity upon field-cooling points to a considerable fraction of pinned uncompensated spins. Such situation is specially favored by its reduced crystallinity, which can eventually manifest through glassy magnetism and a pronounced exchange bias.

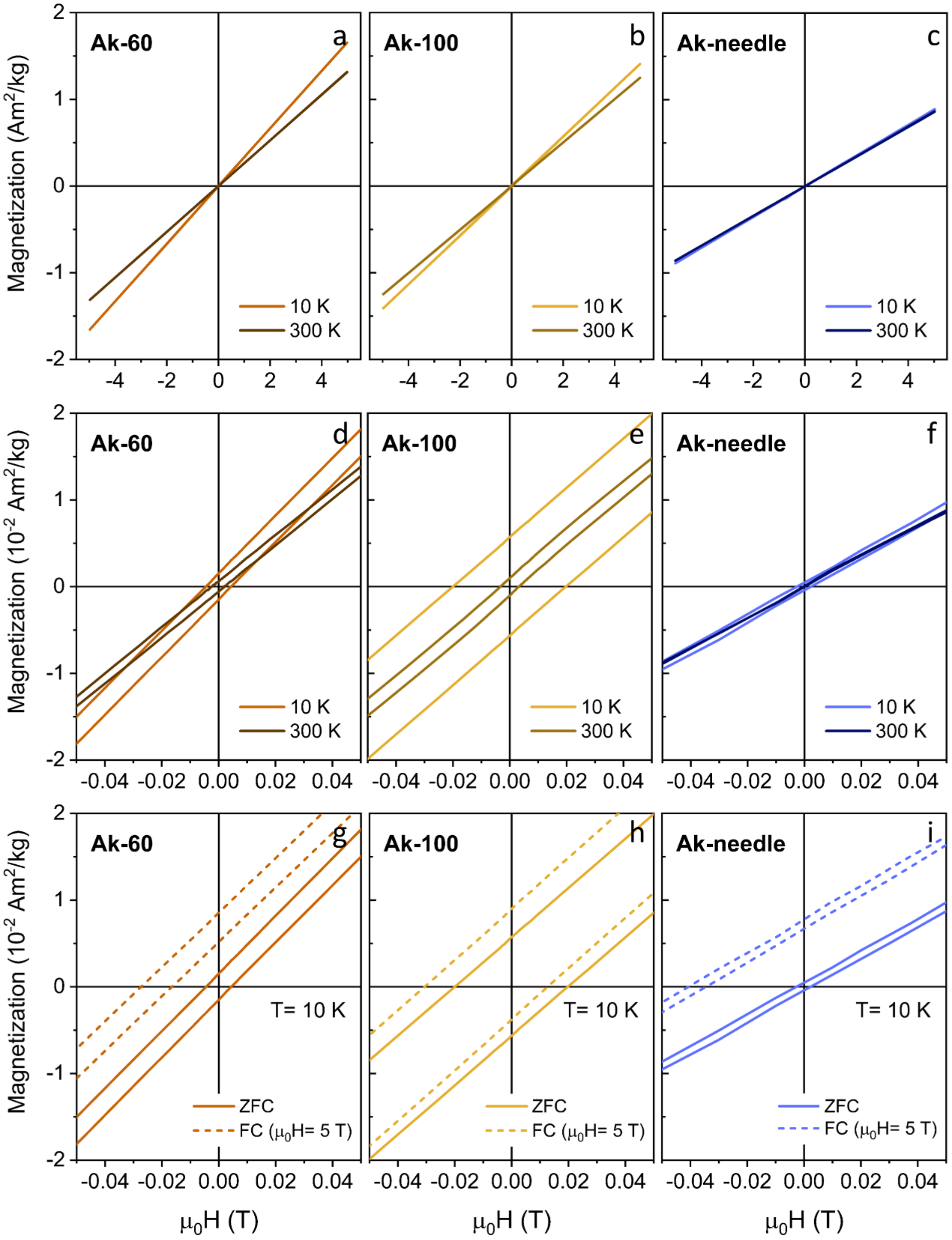

**Figure 5.** Field-dependent magnetization recorded at 10 and 300 K (a, b, c), close-up showing the low field region of the same hysteresis loops (d, e, f), and comparison of the 10 K hysteresis

loops under ZFC and FC ($\mu_0H$= 5 T) conditions (g, h, i) for the Ak-60 (brown), Ak-100 (yellow) and Ak-needle (blue) samples, respectively.

**Table 3.** Summary of the magnetic parameters (at 10 K) for the three akaganéite samples synthesized.

| Sample | $M_{(5\ T)}$ ($Am^2kg^{-1}$) | $\mu_0H_{C\ (ZFC)}$ (mT) | $\mu_0H_{E\ (FC\ 5\ T)}$ (mT) | $\chi_{AFM}$ |
|---|---|---|---|---|
| Ak-60 | 1.65 | 4.4 | -21.9 | $1.47\cdot10^{-3}$ |
| Ak-100 | 1.41 | 19.9 | -9.0 | $1.26\cdot10^{-3}$ |
| Ak-needle | 0.89 | 2.5 | -37.6 | $0.78\cdot10^{-3}$ |

**3.4. Chloride Anion Exchange.** Since the $Cl^-$ anions allocate at the tunnel sites of the akaganéite structure, it is expected that a set of different ions of an adequate size may occupy these interstices as well.[42,58,59] Motivated by the crucial structural and magnetic implications of the interstitial $Cl^-$ content, these anions were exchanged with hydroxide ($OH^-$) ions via a chemical wet method. To this end, an aqueous dispersion of the Ak-100 sample was heated to 55 °C in the presence of NaOH, and the anion exchange was allowed to proceed for 3 hours. A low reaction temperature was selected to prevent the akaganéite dissolution and reprecipitation as hematite or goethite under alkaline conditions.

The TEM characterization of the resultant sample (hereafter denoted as Ak-100-OH) is included in Figure 6a, which confirms the unaltered morphology of the Ak-100 nanostructures in terms of size and porosity. A comparison of the Raman spectrum before and after the anion exchange process is displayed in Figure 6b. The obtained results evidence that the akaganéite crystal structure is preserved, with only minor changes involving the relative intensity of the bands at 386 and 414 $cm^{-1}$. In agreement with the earlier Raman analysis, the lower $I_{386}/I_{414}$ ratio determined for Ak-100-OH (1.21 in contrast to 1.33 for the pristine Ak-100 sample) points to an effective removal of some interstitial $Cl^-$ ions. These crystallographic modifications within the inner channels are also reflected in the sample thermal stability, as shown in Figure 6c. The laser power-dependent Raman spectra (systematically recorded from the same spot in the sample) reveal the presence of the akaganéite phase up to 8.1 mW, whereas in the Ak-100 case the akaganéite crystal structure could only be retained up to 1.8 mW. Similar observations were made by Cai et al., supported by differential scanning calorimetry (DSC) measurements.[31] The enhanced thermal stability of the $OH^-$ and $F^-$-exchanged samples was explained considering the ability of the interstitial ion to bind to the akaganéite framework, which was directly correlated with its electronegativity. In line with this study, in our case the $OH^-$ anions are believed to confer stability by strengthening the hydrogen bonding scheme within the inner channels.

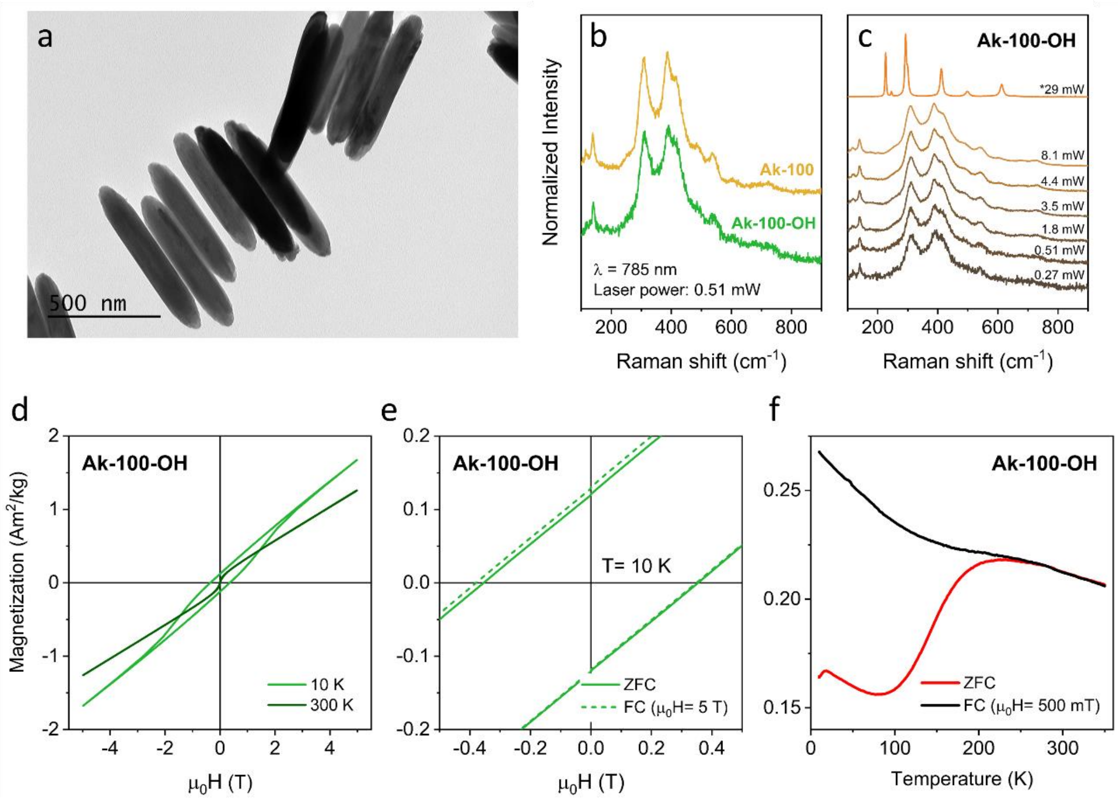

**Figure 6.** (a) Representative TEM image from the Ak-100-OH sample. (b) Comparison of the Raman spectrum of the Ak-100 sample before and after anion exchange; and (c) laser power-dependent Raman spectra obtained from the Ak-100-OH sample. Magnetic characterization of the exchanged sample: (d) field-dependent magnetization at 10 and 300 K; (e) close-up of the ZFC and FC ($\mu_0 H$= 5 T) hysteresis loops (at 10 K) around the low field region; and (f) ZFC-FC curves registered under a constant 500 mT magnetic field.

The magnetic properties of the Ak-100-OH sample are summarized in Figure 6d-f. In addition to the antiferromagnetic contribution inherent to the akaganéite phase, the MH loops presented in Figure 6d depict a strong ferromagnetic-like contribution in the exchanged sample. The coercivity at 10 K is measured to be 354.3 mT, which represents an ~18-fold increase with respect to the Ak-100 sample. Interestingly, no coercivity is observed in the loop registered at 300 K, displaying instead the characteristic S-shape indicative of superparamagnetic behavior. The presence of a SPM component can be equally evidenced from the ZFC-FC curves (see Figure 6f), given the emergence of a clear blocking temperature at 230 K (as determined from the derivative of the ZFC trace). This feature reminds of the Morin transition ($T_M$) in hematite ($\alpha$-$Fe_2O_3$), with a reported value of 260 K for the bulk material.[47] However, the presence of hematite and its assignment to the Morin transition can be discarded because of several reasons: (i) no hematite traces were detected in the structural Raman analysis; (ii) the thermal evolution of the Ak-100-OH magnetic parameters (Figure S6d) shows that the coercivity vanishes above 250 K, hence confirming that the maximum in the ZFC curve corresponds to the blocking temperature of a SPM component; and (iii) there are no profound changes in the antiferromagnetic susceptibility (see corresponding values in Table 4).

Additionally, a subtle peak can be observed at 18 K in the ZFC curve, likely stemming from the blocking temperature of smaller crystalline domains within the nanostructures. A similar blocking temperature was reported by Millan et al. in akaganéite polymer nanocomposites.[35] In that study, the emergence of a clear $T_B$ at 18 K could only be observed after an extensive washing of the akaganéite sample (equivalent to a $Cl^-$ deficiency), while the corresponding $T_B$ in the unwashed sample was claimed to be <2 K. The emergence of two relaxation effects with well-differentiated anisotropies unveils a correlated spin disorder scenario in the Ak-100-OH sample involving two distinct magnetic contributions: one with an associated $T_B$ of 18 K that presumably accounts for the exchange bias phenomenon at 10 K (highlighted in Figure 6e), and a higher magnetic anisotropy component with an associated $T_B$ of 230 K, which becomes responsible for the vanishing of the coercivity above 250 K (refer to Figure S6d).

**Table 4.** Comparison of the magnetic parameters (at 10 K) for the Ak-100 sample before and after anion exchange.

| Sample | $M_{(5\,T)}$ ($Am^2kg^{-1}$) | $\mu_0 H_{C\,(ZFC)}$ (mT) | $\mu_0 H_{E\,(FC\,5\,T)}$ (mT) | $\chi_{AFM}$ |
|---|---|---|---|---|
| Ak-100 | 1.41 | 19.9 | -9.0 | $1.26\cdot10^{-3}$ |
| Ak-100-OH | 1.67 | 354.3 | -15.8 | $1.51\cdot10^{-3}$ |

All things considered, these results prove the crucial role of the $Cl^-$ anions from a structural standpoint, and demonstrate how its substitution with $OH^-$ ions affects the akaganéite thermal stability and modifies the magnetic landscape. Owing to the different size and electronegativity of the two types of anions involved, the exchange process is expected to alter the inner channels microstructure (for instance by changing the interatomic distances of the $Fe(O,OH)_6$ octahedra) and consequently modulate the Fe-O-Fe superexchange interactions. Contrary to Ak-100, the appearance of superparamagnetism in the Ak-100-OH sample evidences that the chemically-induced crystallographic changes boost the occurrence of correlated spin disorder, providing a much stronger source of local magnetic ordering.

## 4. CONCLUSIONS

The study herein presented unveils new mechanistic insights about the preparation of anisotropic akaganéite nanocrystals, taking an important step towards a rational design of nanoparticles *à la carte*. The role of various experimental parameters such as precursor concentration, pH, hydrolysis temperature and aging time is disclosed, which is demonstrated to dictate the nucleation stage and boost a diffusion- or surface-controlled growth depending on the particular synthetic conditions. As a result, spindle-, rod- or needle-like nanostructures can be synthesized in the absence of any shape-control or capping agent, spanning a wide range of sizes from the nanoscale to the submicron- or even microscale. An in-depth Raman spectroscopy analysis unearths the paramount importance of the $Cl^-$ anions not only at directing the anisotropic growth, but also at stabilizing the akaganéite crystal structure via hydrogen bonding within the inner channels.

From a magnetic perspective, the as-prepared nanocrystals exhibit a bulk-like AFM behavior, as well as the appearance of a FM contribution which does not correlate with the particle size nor the surface-to-volume ratio. Contrary to the traditionally assumed magnetic core-shell model, the unexpected magnetism observed is ascribed to inner (bulk) uncompensated spins induced by the different interstitial $Cl^-$ content. As a proof of concept, the crystallographic arrangement within the akaganéite tunnel structure was modified via anion exchange, inducing a SPM behavior which brings about an almost 20-fold increase in coercivity at low temperatures. Due to all the above, this work constitutes the first study to directly and unambiguously address the true magnetic implications of the interstitial ions in β-FeOOH nanostructures, both in a pre- and post-synthetic manner. Moreover, it highlights the rich magnetism that portrays magnetic defect engineering in antiferromagnets, paving the road for their implementation in magnetic memories and a large number of state-of-the-art spintronic and magnonic concepts.

## ASSOCIATED CONTENT

### Supporting Information

The Supporting Information is available free of charge at XXXX.

Additional TEM images showing the assembly into rafts and the effect of precursor concentration; high-resolution TEM characterization; Raman spectra deconvolution; supplementary magnetic data.

## AUTHOR INFORMATION

### Corresponding Author

Martín Testa-Anta; orcid.org/0000-0003-4437-2589. E-mail: mtesta@icmab.es

### Authors

Ecem Tiryaki; orcid.org/0000-0002-9746-0825
Laura Bocher; orcid.org/0000-0002-9589-8743
Verónica Salgueiriño; orcid.org/0000-0002-9396-468X

### Notes

The authors declare no competing financial interest.

## ACKNOWLEDGMENTS

M. T.-A. and E. T. acknowledge financial support from Xunta de Galicia (Regional Government, Spain) under grants ED481A-2017/377 and ED481A-2019/244. V. S. acknowledges financial support from the Spanish Ministerio de Ciencia e Innovación under project PID2020-119242-I00 and from the European Union under project PEPSA-MATE-872233. This project has been partly funded by the European Union's Horizon 2020 research and innovation program under grant agreement No. 823717 (ESTEEM3).

## REFERENCES

(1) Železný, J.; Wadley, P.; Olejník, K.; Hoffmann, A.; Ohno, H. Spin Transport and Spin Torque in Antiferromagnetic Devices. *Nat. Phys.* **2018**, *14* (3), 220–228.

(2) Jungwirth, T.; Marti, X.; Wadley, P.; Wunderlich, J. Antiferromagnetic Spintronics. *Nat. Nanotechnol.* **2016**, *11* (3), 231–241.

(3) Kimel, A. V.; Ivanov, B. A.; Pisarev, R. V.; Usachev, P. A.; Kirilyuk, A.; Rasing, T. Inertia-Driven Spin Switching in Antiferromagnets. *Nat. Phys.* **2009**, *5* (10), 727–731.

(4) DuttaGupta, S.; Kurenkov, A.; Tretiakov, O. A.; Krishnaswamy, G.; Sala, G.; Krizakova, V.; Maccherozzi, F.; Dhesi, S. S.; Gambardella, P.; Fukami, S.; Ohno, H. Spin-Orbit Torque Switching of an Antiferromagnetic Metallic Heterostructure. *Nat. Commun.* **2020**, *11* (1), 5715.

(5) Chen, X.; Zhou, X.; Cheng, R.; Song, C.; Zhang, J.; Wu, Y.; Ba, Y.; Li, H.; Sun, Y.; You, Y.; Zhao, Y.; Pan, F. Electric Field Control of Néel Spin–Orbit Torque in an Antiferromagnet. *Nat. Mater.* **2019**, *18* (9), 931–935.

(6) Gomonay, O.; Jungwirth, T.; Sinova, J. High Antiferromagnetic Domain Wall Velocity Induced by Néel Spin-Orbit Torques. *Phys. Rev. Lett.* **2016**, *117* (1), 017202.

(7) Hijnen, N.; Clegg, P. S. Simple Synthesis of Versatile Akaganéite-Silica Core–Shell Rods. *Chem. Mater.* **2012**, *24* (17), 3449–3457.

(8) Zhu, T.; Li Ong, W.; Zhu, L.; Wei Ho, G. $TiO_2$ Fibers Supported β-FeOOH Nanostructures as Efficient Visible Light Photocatalyst and Room Temperature Sensor. *Sci. Rep.* **2015**, *5* (1), 10601.

(9) Jung, J.; Song, K.; Bae, D. R.; Lee, S. W.; Lee, G.; Kang, Y.-M. β-FeOOH Nanorod Bundles with Highly Enhanced Round-Trip Efficiency and Extremely Low Overpotential for Lithium-Air Batteries. *Nanoscale* **2013**, *5* (23), 11845–11849.

(10) Yusan, S. (Doyurum); Akyil, S. Sorption of Uranium(VI) from Aqueous Solutions by Akaganeite. *J. Hazard. Mater.* **2008**, *160* (2), 388–395.

(11) Urtizberea, A.; Luis, F.; Millán, A.; Natividad, E.; Palacio, F.; Kampert, E.; Zeitler, U. Thermoinduced Magnetic Moment in Akaganéite Nanoparticles. *Phys. Rev. B* **2011**, *83* (21), 214426.

(12) Luna, C.; Ilyn, M.; Vega, V.; Prida, V. M.; González, J.; Mendoza-Reséndez, R. Size Distribution and Frustrated Antiferromagnetic Coupling Effects on the Magnetic Behavior of Ultrafine Akaganéite (β-FeOOH) Nanoparticles. *J. Phys. Chem. C* **2014**, *118* (36), 21128–21139.

(13) Khalid, H.; Heo, S. G.; Yang, W. S.; Kim, B. S.; Kim, T.-S.; Seo, S.-J. Synthesis of 1-D

Iron Oxide Nano-Sticks: Tuning the Interfacial Defects and Surface of Nano-Sticks for Fine-Tuned Exchange Biasing. *J. Alloys Compd.* **2019**, *801*, 199–207.

(14) Mariño-Fernández, R.; Masunaga, S. H.; Fontaíña-Troitiño, N.; Morales, M. P.; Rivas, J.; Salgueirino, V. Goethite (α-FeOOH) Nanorods as Suitable Antiferromagnetic Substrates. *J. Phys. Chem. C* **2011**, *115* (29), 13991–13999.

(15) Tadic, M.; Milosevic, I.; Kralj, S.; Mbodji, M.; Motte, L. Silica-Coated and Bare Akaganeite Nanorods: Structural and Magnetic Properties. *J. Phys. Chem. C* **2015**, *119* (24), 13868–13875.

(16) White, J. S.; Bator, M.; Hu, Y.; Luetkens, H.; Stahn, J.; Capelli, S.; Das, S.; Döbeli, M.; Lippert, T.; Malik, V. K.; Martynczuk, J.; Wokaun, A.; Kenzelmann, M.; Niedermayer, C.; Schneider, C. W. Strain-Induced Ferromagnetism in Antiferromagnetic $LuMnO_3$ Thin Films. *Phys. Rev. Lett.* **2013**, *111* (3), 037201.

(17) Hu, X.; Zhao, Y.; Shen, X.; Krasheninnikov, A. V.; Chen, Z.; Sun, L. Enhanced Ferromagnetism and Tunable Magnetism in $Fe_3GeTe_2$ Monolayer by Strain Engineering. *ACS Appl. Mater. Interfaces* **2020**, *12* (23), 26367-26373.

(18) Wang, F.; Mathur, N.; Janes, A. N.; Sheng, H.; He, P.; Zheng, X.; Yu, P.; DeRuiter, A. J.; Schmidt, J. R.; He, J.; Jin, S. Defect-Mediated Ferromagnetism in Correlated Two-Dimensional Transition Metal Phosphorus Trisulfides. *Sci. Adv.* **2021**, *7* (43), eabj4086.

(19) Sugiyama, I.; Shibata, N.; Wang, Z.; Kobayashi, S.; Yamamoto, T.; Ikuhara, Y. Ferromagnetic Dislocations in Antiferromagnetic NiO. *Nat. Nanotechnol.* **2013**, *8* (4), 266–270.

(20) Chen, C.; Li, H.; Seki, T.; Yin, D.; Sanchez-Santolino, G.; Inoue, K.; Shibata, N.; Ikuhara, Y. Direct Determination of Atomic Structure and Magnetic Coupling of Magnetite Twin Boundaries. *ACS Nano* **2018**, *12* (3), 2662–2668.

(21) Fontaiña-Troitiño, N.; Ramos-Docampo, M. A.; Testa-Anta, M.; Rodríguez-González, B.; Bañobre-López, M.; Bocher, L.; McKenna, K. P.; Salgueiriño, V. Antiphase Boundaries in Truncated Octahedron-Shaped Zn-Doped Magnetite Nanocrystals. *J. Mater. Chem. C* **2018**, *6* (47), 12800–12807.

(22) Veremchuk, I.; Liedke, M. O.; Makushko, P.; Kosub, T.; Hedrich, N.; Pylypovskyi, O. V.; Ganss, F.; Butterling, M.; Hübner, R.; Hirschmann, E.; Attallah, A. G.; Wagner, A.; Wagner, K.; Shields, B.; Maletinsky, P.; Fassbender, J.; Makarov, D. Defect Nanostructure and Its Impact on Magnetism of α-$Cr_2O_3$ Thin Films. *Small* **2022**, *18* (17), 2201228.

(23) Bencan, A.; Drazic, G.; Ursic, H.; Makarovic, M.; Komelj, M.; Rojac, T. Domain-Wall Pinning and Defect Ordering in $BiFeO_3$ Probed on the Atomic and Nanoscale. *Nat. Commun.* **2020**, *11* (1), 1762.

(24) Jourdan, T.; Lançon, F.; Marty, A. Pinning of Magnetic Domain Walls to Structural Defects in Thin Layers within a Heisenberg-Type Model. *Phys. Rev. B* **2007**, *75* (9), 094422.

(25) Han, H.; Yao, Y.; Robinson, R. D. Interplay between Chemical Transformations and Atomic Structure in Nanocrystals and Nanoclusters. *Acc. Chem. Res.* **2021**, *54* (3), 509–519.

(26) Otero-Martínez, C.; Imran, M.; Schrenker, N. J.; Ye, J.; Ji, K.; Rao, A.; Stranks, S. D.; Hoye, R. L. Z.; Bals, S.; Manna, L.; Pérez-Juste, J.; Polavarapu, L. Fast A-Site Cation Cross-

Exchange at Room Temperature: Single-to Double- and Triple-Cation Halide Perovskite Nanocrystals. *Angew. Chemie Int. Ed.* **2022**, *61* (34), e202205617.

(27) Nelson, A.; Honrao, S.; Hennig, R. G.; Robinson, R. D. Nanocrystal Symmetry Breaking and Accelerated Solid-State Diffusion in the Lead–Cadmium Sulfide Cation Exchange System. *Chem. Mater.* **2019**, *31* (3), 991–1005.

(28) Nedelcu, G.; Protesescu, L.; Yakunin, S.; Bodnarchuk, M. I.; Grotevent, M. J.; Kovalenko, M. V. Fast Anion-Exchange in Highly Luminescent Nanocrystals of Cesium Lead Halide Perovskites ($CsPbX_3$, X = Cl, Br, I). *Nano Lett.* **2015**, *15* (8), 5635–5640.

(29) Lentijo-Mozo, S.; Deiana, D.; Sogne, E.; Casu, A.; Falqui, A. Unexpected Insights about Cation-Exchange on Metal Oxide Nanoparticles and Its Effect on Their Magnetic Behavior. *Chem. Mater.* **2018**, *30* (21), 8099–8112.

(30) Wu, C.; Dang, Z.; Pasquale, L.; Wang, M.; Colombo, M.; De Trizio, L.; Manna, L. Hollowing of MnO Nanocrystals Triggered by Metal Cation Replacement: Implications for the Electrocatalytic Oxygen Evolution Reaction. *ACS Appl. Nano Mater.* **2021**, *4* (6), 5904–5911.

(31) Cai, J.; Liu, J.; Gao, Z.; Navrotsky, A.; Suib, S. L. Synthesis and Anion Exchange of Tunnel Structure Akaganeite. *Chem. Mater.* **2001**, *13* (12), 4595–4602.

(32) Chambaere, D.; De Grave, E. On the Néel Temperature of βFeOOH: Structural Dependence and Its Implications. *J. Magn. Magn. Mater.* **1984**, *42* (3), 263–268.

(33) Kasparis, G.; Erdocio, A. S.; Tuffnell, J. M.; Thanh, N. T. K. Synthesis of Size-Tuneable β-

FeOOH Nanoellipsoids and a Study of Their Morphological and Compositional Changes by Reduction. *CrystEngComm* **2019**, *21* (8), 1293–1301.

(34) Zhu, T.; Chen, J. S.; Lou, X. W. (David). Glucose-Assisted One-Pot Synthesis of FeOOH Nanorods and Their Transformation to $Fe_3O_4$@Carbon Nanorods for Application in Lithium Ion Batteries. *J. Phys. Chem. C* **2011**, *115* (19), 9814–9820.

(35) Millan, A.; Urtizberea, A.; Natividad, E.; Luis, F.; Silva, N. J. O.; Palacio, F.; Mayoral, I.; Ruiz-González, M. L.; González-Calbet, J. M.; Lecante, P.; Serin, V. Akaganeite Polymer Nanocomposites. *Polymer (Guildf).* **2009**, *50* (5), 1088–1094.

(36) Bailey, J. K.; Brinker, C. J.; Mecartney, M. L. Growth Mechanisms of Iron Oxide Particles of Differing Morphologies from the Forced Hydrolysis of Ferric Chloride Solutions. *J. Colloid Interface Sci.* **1993**, *157* (1), 1–13.

(37) Matijević, E.; Scheiner, P. Ferric Hydrous Oxide Sols: III. Preparation of Uniform Particles by Hydrolysis of Fe(III)-Chloride, -Nitrate, and -Perchlorate Solutions. *J. Colloid Interface Sci.* **1978**, *63* (3), 509–524.

(38) Bernal, J. D.; Dasgupta, D. R.; Mackay, A. L. The Oxides and Hydroxides of Iron and Their Structural Inter-Relationships. *Clay Miner. Bull.* **1959**, *4* (21), 15–30.

(39) Mackay, A. L. β-Ferric Oxyhydroxide. *Mineral. Mag. J. Mineral. Soc.* **1960**, *32* (250), 545–557.

(40) Post, J. E.; Heaney, P. J.; Von Dreele, R. B.; Hanson, J. C. Neutron and Temperature-Resolved Synchrotron X-Ray Powder Diffraction Study of Akaganéite. *Am. Mineral.* **2003**,

*88* (5–6), 782–788.

(41) Tadic, M.; Milosevic, I.; Kralj, S.; Mitric, M.; Makovec, D.; Saboungi, M.-L.; Motte, L. Synthesis of Metastable Hard-Magnetic ε-$Fe_2O_3$ Nanoparticles from Silica-Coated Akaganeite Nanorods. *Nanoscale* **2017**, *9* (30), 10579–10584.

(42) Villacorta, V.; García, K. E.; Greneche, J.-M.; Barrero, C. A. Influences of As(V), Sb(III), and Hg(II) Ions on the Nucleation and Growth of Akaganeite. *CrystEngComm* **2019**, *21* (46), 7155–7165.

(43) Post, J. E.; Buchwald, V. F. Crystal Structure Refinement of Akaganéite. *Am. Mineral.* **1991**, *76* (1–2), 272–277.

(44) Réguer, S.; Neff, D.; Bellot-Gurlet, L.; Dillmann, P. Deterioration of Iron Archaeological Artefacts: Micro-Raman Investigation on Cl-Containing Corrosion Products. *J. Raman Spectrosc.* **2007**, *38* (4), 389–397.

(45) Neff, D.; Bellot-Gurlet, L.; Dillmann, P.; Reguer, S.; Legrand, L. Raman Imaging of Ancient Rust Scales on Archaeological Iron Artefacts for Long-Term Atmospheric Corrosion Mechanisms Study. *J. Raman Spectrosc.* **2006**, *37* (10), 1228–1237.

(46) Font, E.; Carlut, J.; Rémazeilles, C.; Mather, T. A.; Nédélec, A.; Mirão, J.; Casale, S. End-Cretaceous Akaganéite as a Mineral Marker of Deccan Volcanism in the Sedimentary Record. *Sci. Rep.* **2017**, *7* (1), 11453.

(47) Testa-Anta, M.; Ramos-Docampo, M. A.; Comesaña-Hermo, M.; Rivas-Murias, B.; Salgueiriño, V. Raman Spectroscopy to Unravel the Magnetic Properties of Iron Oxide

Nanocrystals for Bio-Related Applications. *Nanoscale Adv.* **2019**, *1* (6), 2086–2103.

(48) de Faria, D. L. A.; Venâncio Silva, S.; de Oliveira, M. T. Raman Microspectroscopy of Some Iron Oxides and Oxyhydroxides. *J. Raman Spectrosc.* **1997**, *28* (11), 873–878.

(49) Ståhl, K.; Nielsen, K.; Jiang, J.; Lebech, B.; Hanson, J. C.; Norby, P.; van Lanschot, J. On the Akaganéite Crystal Structure, Phase Transformations and Possible Role in Post-Excavational Corrosion of Iron Artifacts. *Corros. Sci.* **2003**, *45* (11), 2563–2575.

(50) Li, S.; Hihara, L. H. A Micro-Raman Spectroscopic Study of Marine Atmospheric Corrosion of Carbon Steel: The Effect of Akaganeite. *J. Electrochem. Soc.* **2015**, *162* (9), C495–C502.

(51) Song, X.; Boily, J.-F. Surface and Bulk Thermal Dehydroxylation of FeOOH Polymorphs. *J. Phys. Chem. A* **2016**, *120* (31), 6249–6257.

(52) Xavier, A. M.; Ferreira, F. F.; Souza, F. L. Morphological and Structural Evolution from Akaganeite to Hematite of Nanorods Monitored by Ex Situ Synchrotron X-Ray Powder Diffraction. *RSC Adv.* **2014**, *4* (34), 17753–17759.

(53) Peretyazhko, T. S.; Pan, M. J.; Ming, D. W.; Rampe, E. B.; Morris, R. V.; Agresti, D. G. Reaction of Akaganeite with Mars-Relevant Anions. *ACS Earth Space Chem.* **2019**, *3* (2), 314–323.

(54) Tobia, D.; Winkler, E.; Zysler, R. D.; Granada, M.; Troiani, H. E. Size Dependence of the Magnetic Properties of Antiferromagnetic $Cr_2O_3$ Nanoparticles. *Phys. Rev. B* **2008**, *78* (10), 104412.

(55) Tadic, M.; Milosevic, I.; Kralj, S.; Saboungi, M.-L.; Motte, L. Ferromagnetic Behavior and Exchange Bias Effect in Akaganeite Nanorods. *Appl. Phys. Lett.* **2015**, *106* (18), 183706.

(56) Nehme, Z.; Labaye, Y.; Yaacoub, N.; Grenèche, J. M. An Atomic Scale Monte Carlo Study of Exchange Bias in Homogeneous/Inhomogeneous Core/Shell $Fe_3O_4$/CoO Nanoparticles. *J. Nanoparticle Res.* **2019**, *21* (10), 209.

(57) Schuller, I. K.; Morales, R.; Batlle, X.; Nowak, U.; Güntherodt, G. Role of the Antiferromagnetic Bulk Spins in Exchange Bias. *J. Magn. Magn. Mater.* **2016**, *416*, 2–9.

(58) Richmond, W. R.; Hockridge, J. G.; Loan, M.; Parkinson, G. M. A New Iron Oxyhydroxide Phase:  The Molybdate-Substituted Analogue of Akaganéite. *Chem. Mater.* **2004**, *16* (17), 3203–3205.

(59) Song, Y.; Bac, B. H.; Lee, Y.-B.; Kim, M. H.; Kang, I. M. Highly Ordered Ge-Incorporated Akaganeite (β-FeOOH): A Tunnel-Type Nanorod. *CrystEngComm* **2011**, *13* (1), 287–292.

# For Table of Contents Only

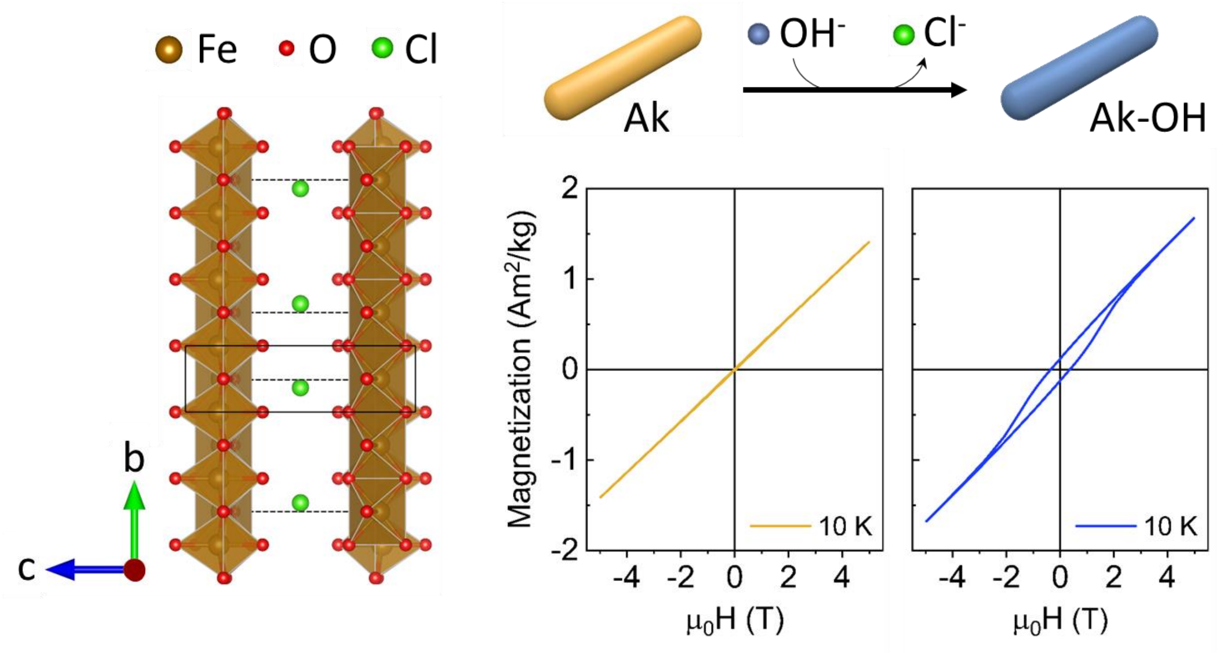
Fe
O
Cl
b
c
OH⁻
Cl⁻
Ak
Ak-OH
Magnetization (Am²/kg)
2
1
0
-1
-2
-4
-2
0
2
4
μ₀H (T)
10 K
-4
-2
0
2
4
μ₀H (T)
10 K